Large-Scale Diagnostics of Tropical Cyclogenesis Potential Using Environment Variability Metrics and Logistic Regression Models

JEFFREY J. WATERS, JENNI L. EVANS, AND CHRIS E. FOREST

The Pennsylvania State University, University Park, Pennsylvania

ABSTRACT

The authors propose that inclusion of medium- to high-frequency variability information will provide improved metrics of tropical cyclogenesis (TCG) applicable to climate GCM diagnostics. Capabilities of the Community Atmosphere Model version 3.1 (CAM3.1) GCM are assessed for detecting both large-scale and localized conditions for TCG in the tropical North Atlantic by comparison with the 40-yr European Centre for Medium-Range Weather Forecasts Re-Analysis (ERA-40) and observed TCG occurrences. CAM3.1 seasonality of large-scale environmental factors conducive to TCG compares favorably with the ERA-40. It is determined that most of the TCG-related high-frequency temporal variability in the ERA-40 is explained by dynamic variability; each of the CAM3.1 ensemble members has lower variability in these dynamic fields. Seventeen environmental variables are evaluated as potential indicators of TCG activity based on daily anomalous variability with respect to a 15-day base period. Principal component analysis (PCA) is employed to synthesize these into a set of uncorrelated parameters. ERA-40 PCA composite variables are used to develop logistic and Poisson regression models for TCG detection and frequency in the North Atlantic main development region. Some skill metrics for the logistic model are promising, but the threat score and hit rate signify that further development of the logistic regression model is warranted; results from the Poisson regression model based on the same inputs are weaker, implying that weighting by TCG counts does not improve the results. These findings indicate merit in incorporating medium- to high-frequency variability in TCG metrics for diagnostics of seasonal activity and for application to climate models.

1. Introduction

Within the tropical cyclone (TC) developmental cycle, the transition from pregenesis/tropical depression status to tropical storm (TS) status is referred to as tropical cyclogenesis (TCG). Thus, TCG is the process of transformation of a "disorganized" convective system into a self-sustaining synoptic-scale warm-core vortex with a cyclonic circulation at the surface (Montgomery and Farrell 1993; Evans 2011). This TCG transition is dependent upon the existence of an initial disturbance in large-scale environmental conditions conducive to vortex spinup via convective feedback (Charney and Eliassen 1964; Ooyama 1964; Emanuel 1986, 1995).

Gray (1968, 1979) identified a set of large-scale environmental conditions conducive for TCG: a preexisting low-level relative vorticity anomaly, minimal wind shear throughout the depth of the troposphere, significant presence of Coriolis rotation, high relative humidity in the midtroposphere, warm sea surface temperatures (SSTs) in a sufficiently deep oceanic mixed layer, and a conditionally unstable atmosphere. These are the basis of the Gray seasonal genesis parameter (section 2c).

Prior to TCG, a finite amplitude disturbance such as an upper-level potential vorticity (PV) anomaly superposed over a low-level disturbance, must exist within the favorable large-scale environment long enough to generate instability (e.g., McBride and Zehr 1981; Emanuel 1986; Challa and Pfeffer 1990). Thus, TCG relies on interactions between large-scale thermodynamic and localized dynamic conditions.

Many studies have attempted to quantify the impact of atmospheric, oceanic, and climatological modulations on TCG and TC activity using general circulation models (GCMs) (e.g., Ryan et al. 1992; Vitart 2006; Camargo

Corresponding author address: Jenni L. Evans, Department of Meteorology, The Pennsylvania State University, 503 Walker Building, University Park, PA 16802.
E-mail: evans@meteo.psu.edu

et al. 2007; Vecchi and Soden 2007; Emanuel et al. 2008). Part of the difficulty in these analyses lies in identifying the initializing factors that represent incipient disturbances or large-scale environmental forcing. Two methodologies have been commonly used for diagnosing and/or forecasting TCG in a GCM for either seasonal forecasting or climate change simulations: (i) detection and tracking of individual TC-like features in a GCM simulation and (ii) inference of TC activity via downscaling.

Previous studies have demonstrated that many low-resolution (T31–T85) climate GCMs produce model "TCs" that exhibit weaker intensities and larger spatial scales than observed TCs (Bengtsson et al. 1982, 2007; Vitart et al. 1997); however, higher resolution GCMs are beginning to resolve more realistic systems (e.g., Oouchi et al. 2006; LaRow et al. 2008; Zhao et al. 2009; Zhao and Held 2010; Gall et al. 2011; Vecchi et al. 2011). Recent diagnostics of low-resolution GCMs demonstrate that, while individual TCs may not be well resolved, when compared to statistically based hindcasts, some GCMs have skill in detecting and tracking TC-like systems on seasonal and interannual time scales (Camargo and Sobel 2004; Camargo et al. 2005, 2007; Vitart et al. 2007). These findings highlight the abilities of low-resolution GCMs to identify dynamic and thermodynamic TCG conditions on spatial scales of relevance to TCG.

We focus here on the method of TCG inference from large-scale environmental variables via downscaling. In this framework, TC activity is inferred from an atmospheric GCM (AGCM) using metrics that characterize the large-scale physics underlying genesis. Our method differs from previous approaches (Ryan et al. 1992; Watterson et al. 1995; Royer et al. 1998; Thorncroft and Pytharoulis 2001; Emanuel and Nolan 2004; McDonnell and Holbrook 2004) in that we use variability metrics of relevant environmental fields, rather than monthly averages, in developing our algorithm for inference of TCG.

Medium- to high-frequency variability measures of a set of atmospheric and oceanic variables are assessed for their relevance to TCG in the North Atlantic main development region (MDR) and a reduced set is retained. Variability is defined in terms of daily anomalies against reference averaging time periods of 10 and 15 days; for the purposes of brevity, we report on the 15-day results here.[1] This base time period is chosen to capture the evolution of active and inactive TCG periods of around 2–3 weeks observed throughout the hurricane season

(e.g., Gray 1988). By applying principal component analysis (PCA), the variables are transformed into an uncorrelated set of composite thermodynamic and dynamic parameters that identifies realistic TCG environments in terms of anomalous variability of daily data. These TCG metrics must also be applicable to the evaluation of environments conducive to TCG from GCM simulations as one of our longer-term goals is to develop variability measures to infer TCG likelihood, rather than using either mean values (e.g., Gray 1979; Emanuel and Nolan 2004; Camargo et al. 2007) or more computationally expensive system-by-system downscaling (e.g., Knutson et al. 2007; Emanuel et al. 2008). Although it is important to predict changes in seasonal TC activity over decadal and longer time scales, in this study we report on the ability of a climate GCM to reproduce environments favorable to TCG.

Details of the data, deviation anomaly (variance) calculations, and verification techniques are provided in section 2. The skill of the Community Atmosphere Model, version 3.1 (CAM3.1) in reproducing monthly (medium frequency) and seasonal variability of the large-scale environment consistent with patterns of observed TCG occurrence is evaluated and is compared with the same diagnostics from the 40-yr European Centre for Medium-Range Weather Forecasts Re-Analysis (ERA-40) dataset (CISL 2011; ECMWF 2011) (see also section 3). After assessing the skill of the CAM3.1 AGCM at reproducing medium-frequency variability and seasonality of the TCG environment, we characterize TCG potential in terms of the high-frequency variability of the TCG environment to capture interactions between thermodynamic and dynamic variables on 15-day time scales (e.g., McBride and Zehr 1981). We relate TCG occurrence to the high-frequency variability of each thermodynamic and dynamic parameter (both individually and in the presence of other variables). As noted above, we employ PCA to condense these metrics of environmental variability into a reduced set of uncorrelated parameters for diagnosing TCG likelihoods (section 4). Finally, logistic and Poisson regression models are developed from the composite parameters to evaluate the likelihood of TCG detection in a 15-day period based on the large-scale environment (section 5). These results are synthesized and discussed in section 6.

2. Data and methodology

a. Focus time period and focus region

Seventeen thermodynamic and dynamic TCG parameters (Table 1) are evaluated over the Atlantic Ocean main development region (9°–21°N, 20°–60°W) for the

---

[1] Parallel analyses for both 10-day and 15-day averaging periods are documented in Waters (2011). The MDR used in the Waters analyses is somewhat larger (9°–21°N, 20°–80°W) than here.

TABLE 1. The set of 17 TCG metrics examined here for inclusion in the summary logistic and Poisson regression models (section 5). Moist IPV is calculated following Schubert et al. (2001).

Variable	Acronym/symbol	Units	Source
McBride and Zehr (1981) daily genesis parameter	DGP	s^{-1}	$(\zeta_{925} - \zeta_{200})$ averaged over a $6° \times 6°$ latitude grid
Daily 310-K IPV	IPV310	$m^2\ s^{-1}\ K\ kg^{-1}$	IPV $= -g(\zeta_\Theta + f)(\partial\theta/\partial p)$
Daily 350-K IPV	IPV350	$m^2\ s^{-1}\ K\ kg^{-1}$	IPV $= -g(\zeta_\Theta + f)(\partial\theta/\partial p)$
Difference of daily 310- and 350-K IPV	IPVDiff	$m^2\ s^{-1}\ K\ kg^{-1}$	Daily 310 K-350 K IPV Difference
200–500-hPa shear of the horizontal wind	Shear 200–500	$m\ s^{-1}$	$\sqrt{[(u_{200}-u_{500})^2 + (v_{200}-v_{500})^2]}$
500–925-hPa shear of the horizontal wind	Shear 500–925	$m\ s^{-1}$	$\sqrt{[(u_{500}-u_{925})^2 + (v_{500}-v_{925})^2]}$
200–925-hPa shear of the horizontal wind	Shear	$m\ s^{-1}$	$\sqrt{[(u_{200}-u_{925})^2 + (v_{200}-v_{925})^2]}$
Daily 310-K moist IPV	IPV310-TV	$m^2\ s^{-1}\ K\ kg^{-1}$	Moist IPV $= -g(\zeta_\Theta + f)(\partial\theta v/\partial p)$
Daily 350-K moist IPV	IPV350-TV	$m^2\ s^{-1}\ K\ kg^{-1}$	Moist IPV $= -g(\zeta_\Theta + f)(\partial\theta v/\partial p)$
Gray (1979) vorticity parameter	ζ_{850}	s^{-1}	850-hPa relative vorticity
Sea level pressure	SLP	hPa	Model variable
500-hPa vertical velocity	W_{500}	hPa day^{-1}	Model variable
Surface convective precipitation rate	PR	mm day^{-1}	Model variable
Gray (1979) moist stability parameter	Instability	K (500 hPa)$^{-1}$	Surface–500-hPa moist instability
Gray (1979) humidity parameter	RH$_{700-500}$	%	700–500-hPa average relative humidity
500-hPa temperature	T_{500}	K	Model variable
700-hPa equivalent potential temperature (θ_e)	ThetaE700	K	$\theta_e = T(1000/P)^{0.286} + 3w$ T: temperature (K) P: pressure (hPa) w: mixing ratio (g kg^{-1})

months of June–September 1981–2000. The MDR is source region for around 50% of Atlantic TC activity in these months (Goldenberg and Shapiro 1996). For reference, 69 named TCs formed in the MDR during the 20-yr June–September study time period (Figs. 1a and 2).

b. Reanalysis dataset and atmospheric GCM used

Diagnostics of the ERA-40 reanalyses are compared with an ensemble of twentieth-century simulations from the CAM3.1 AGCM. The ERA-40 reanalyses span the period from mid-1957 through to 2001 with a spatial grid scale equivalent of $1.4° \times 1.4°$ resolution in the tropics, similar to the resolution of the AGCM studied here. Similar resolutions are used between the models in order to give the CAM3.1 the best chance of capturing details represented in the reanalyses.

The CAM3.1 is the atmospheric component of the fully coupled Community Climate System Model, version 3 (CCSM3) (Collins et al. 2004). Previous studies (e.g., Wehner et al. 2010; Smirnov and Vimont 2011) have demonstrated that the CAM3.1 is a reasonable model for research in tropical cyclone statistics and variability, although it has biases in annual precipitation rates (Sobel et al. 2009) and deep convective precipitation

patterns (Zhang et al. 2010). To study the potential for simulation of the TCG environment in CAM3.1, we create a four-member ensemble (denoted here as IC1 through IC4) forced with observed monthly averaged SSTs from 1979 to 2000, but initialized with data from different dates. CAM3.1 is run at T85 resolution ($1.4° \times 1.4°$) with 26 levels in a hybrid terrain-following sigma-pressure coordinate. This four-member ensemble reflects a portion of the uncertainty that is commonly associated with the AGCM output. Analyses presented for these simulations span the 20-yr period 1981–2000; results are output on daily and monthly time scales. Two extra years (1979–80) are included at the onset of each simulation to allow for model spinup to eliminate effects of the initial conditions on the model.

c. Seasonal diagnostics of TCG potential

To characterize the distribution of TC activity in the present climate, Gray (1979) developed the empirical diagnostic seasonal genesis parameter [SGP, Eq. (1)]. The SGP comprises six variables. Three thermodynamic variables combine to detect the ability of the environment to support active deep convection: 1) ocean thermal energy $[\int \rho_w c_w (T - 26)\, dz]$ for water temperatures
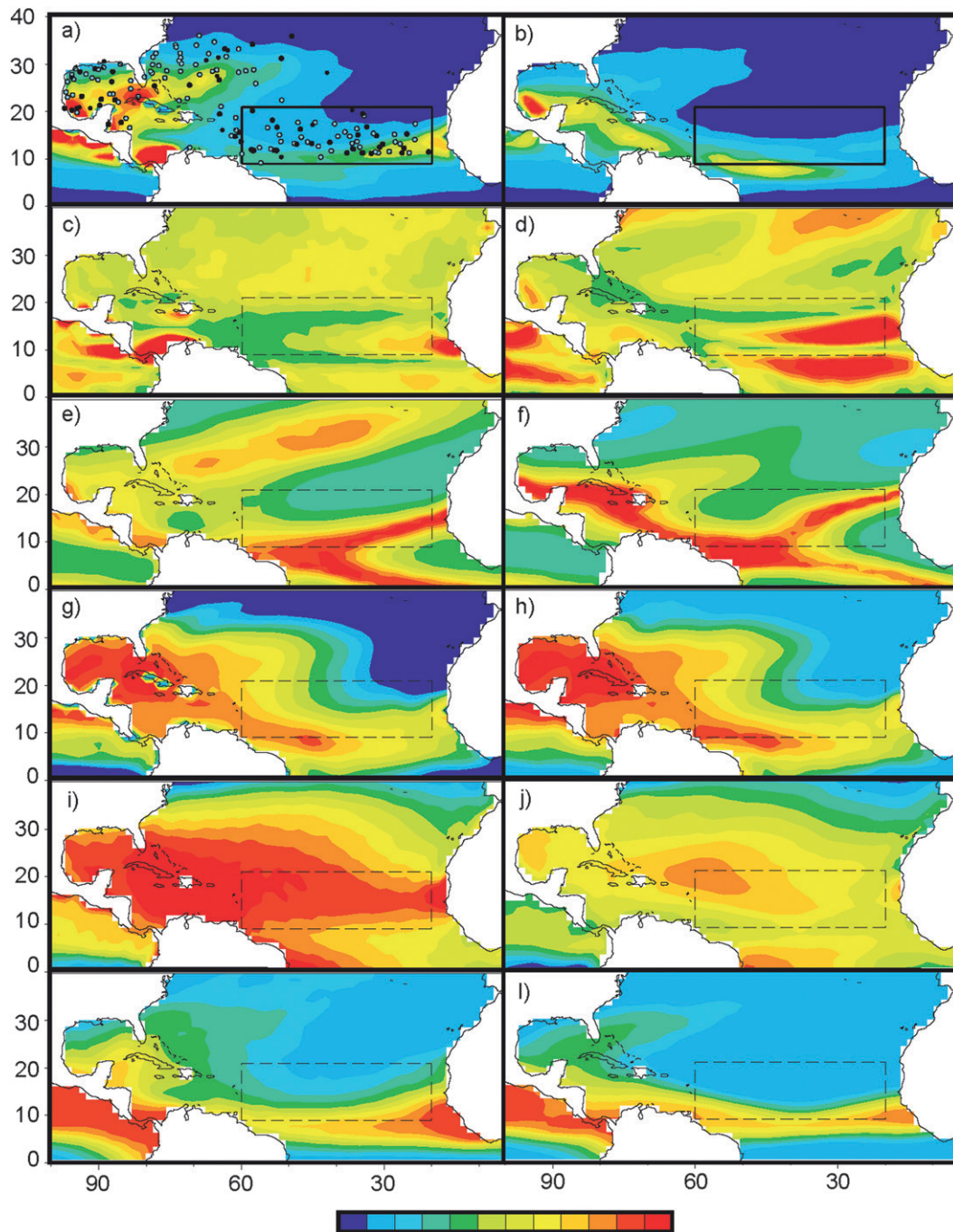
FIG. 1. SGP and component terms for the 1981–2000 mean September for the (left column) ERA-40 and (right column) CAM3.1: (a),(b) SGP, (c),(d) 850-hPa relative vorticity, (e),(f) inverse of 200–925-hPa shear, (g),(h) ocean thermal energy, (i),(j) surface to 500-hPa moist instability, and (k),(l) 700–500-hPa relative humidity. The relative humidity term is zero for RH $\leq$ 40% and 1 for RH $\geq$ 70%. Regions conducive to TCG based on that metric (red) and regions adverse to TCG (dark blue) are indicated. Contour intervals are the same for both models for each variable. Values range from 0 to 10 TCG events per 20 yr for the SGP, 0 to 2 ($\times 10^{-5}$ s^{-1}) for relative vorticity, 0 to 0.3 m s^{-1} (750 hPa)$^{-1}$ for shear, 2×10^4 Cal cm^{-2} (1 Cal cm^{-2} = 41 841 J m^{-2}) for thermal energy, and 0 to 15 K (500 hPa)$^{-1}$ for instability. See Table 1 for definitions and method of calculation for all terms. The box in each panel [emphasized in (a)] delineates the main development region (MDR) analyzed in this study. Observed genesis locations for the 20-yr period are plotted in (a): TCG events occurring in September (the month diagnosed in this figure are plotted as solid black circles and all other TCG events in these 20 years as open circles.

FIG. 2. Observed TCG occurrences within the MDR for each of the 160 15-day base periods over June–September 1981–2000. The occurrence of at least one TCG event during a particular 15-day period (open bars), and the total number of TCG events that occurred during a particular 15-day period (solid bars) are shown. This information provides the response variable for the development of the regression models reported in section 5.

in excess of 26°C to a depth of 60 m, 2) moist instability ($\partial \theta_e / \partial p$) for difference in equivalent potential temperature between the surface and 500 hPa, and 3) relatively high midtroposphere relative humidity (RH). Three dynamic variables characterize the ability of an incipient disturbance to focus the latent heating resulting from this convection: 1) relative vorticity from the surface to 850-hPa (ζ_r), 2) latitudinal Coriolis parameter (f), and 3) the inverse of the vertical shear of the horizontal winds over the depth of the free troposphere between 925 and 200 hPa (S_z^{-1}). Gray defined the SGP as

$$\text{SGP} = (|\zeta_r| + 5)|f|\left(\frac{1}{S_z + 3}\right)\left[\iint \rho_w c_w (T - 26)\, dz\right]$$
$$\times \left[\left(\frac{\partial \theta_e}{\partial p}\right) + 5\right]\left(\frac{\text{RH} - 40}{30}\right). \qquad (1)$$

The SGP captures the seasonality and relative frequencies of TCG across all major ocean basins (Gray 1979) and has been used to trace the effects of large-scale interannual variability (e.g., El Niño) on seasonal TCG frequencies (Clark and Chu 2002). Several investigations (Ryan et al. 1992; Watterson et al. 1995; Walsh and Watterson 1997; Royer et al. 1998) have employed the SGP to evaluate the tropical climate variables relevant for TCG in control GCM simulations and such inferred potential changes in TC activity in alternate climate regimes. Such experiments have highlighted the strong sensitivity of the SGP to SST through both the ocean thermal energy and the moist instability parameters.

McBride and Zehr (1981) partitioned the six SGP terms into two subsets: thermal potential and dynamical potential for TCG. They noted that only dynamical parameters possess significant day-to-day variations throughout a TC season. As a result, they attributed the SGP thermodynamic parameters to the seasonality of TCG and the SGP dynamical parameters to daily TCG potential. They concluded that TCG is a result of large-scale flow changes in the tropical environment rather than the properties of the incipient disturbance. These results helped motivate the medium to high-frequency diagnostics of large-scale dynamical fields explored here.

Emanuel and Nolan (2004) proposed a genesis potential index [GPI, Eq. (2)] as an advance on the SGP. The GPI essentially incorporates the same parameters as the SGP but avoids the "SST threshold trap" by employing TC potential intensity, denoted V_{pot}, as a measure of the thermodynamic support for TCG (Emanuel 1986). The other parameters incorporated in the GPI are the 850-hPa absolute vorticity (η), 700-hPa relative humidity (H), and 850–200-hPa wind shear of the horizontal winds (V_{shear}). An empirical fit to observed TC records was used to derive the equation defining the nondimensional GPI:

$$\text{GPI} = |10^5 \eta|^{3/2}\left(\frac{H}{50}\right)^3\left(\frac{V_{\text{pot}}}{70}\right)^3 (1 + 0.1 V_{\text{shear}})^{-2}. \qquad (2)$$

The GPI has been used to evaluate the skill of GCMs in reproducing interannual spatial variations of seasonal

TCG (Camargo et al. 2007; Yokoi et al. 2009) for the current climate. These GCMs were determined to exhibit skill at reproducing the observed seasonal phasing and timing of GPI across many oceanic regions; however, the magnitudes and spatial domains of the GPI maxima often differed from the validating reanalysis data.

In section 3a, we employ the SGP and GPI to evaluate the spatially varying seasonal evolution of the CAM3.1 tropical Atlantic in comparison with the ERA-40.

d. Large-scale diagnostics to infer medium- to high-frequency variability of TCG

Application of the SGP and GPI diagnostics to the ERA-40 over the 20-yr study period provides spatial distributions of TCG potential on seasonal time scales (section 3a). However, recent studies have demonstrated the importance of the phase of the Madden–Julian oscillation (MJO) and equatorial wave activity to medium to high-frequency TCG variability (e.g., Frank and Roundy 2006; Aiyyer and Molinari 2008). These structures in the tropical atmosphere modulate the dynamic and thermodynamic structure of the large-scale environment, impacting the potential for TCG locally in space and time. While GCMs have shown only limited skill simulating the MJO (Randall et al. 2007) and moist equatorial waves (e.g., Straub et al. 2010), considerations of the environmental anomalies associated with the MJO and equatorial waves informed our selection of candidate variables designed to capture TCG on time scales from days to weeks (section 3b, Table 1).

Eleven metrics of the medium to high-frequency variability of TCG dynamic potential are examined here (Table 1): 1) the McBride and Zehr (1981) daily genesis parameter (DGP), defined as the area-integrated difference between the 925-hPa and 200-hPa relative vorticity; 2) isentropic potential vorticity (IPV) in the lower troposphere (310 K); 3) upper-troposphere (350 K) IPV; and 4) the strength of IPV difference between these two levels. Environmental vertical wind shear is calculated over three different layers: 5) deep (925–200 hPa) layer shear, and 6) upper (500–200 hPa)- and 7) lower (925–500 hPa) tropospheric shear. In addition, moist IPV (Schubert et al. 2001) is calculated at 8) 310 K (IPV310-T_V) and 9) 350 K (IPV350-T_V). The final two variables calculated are 10) the SGP vorticity parameter (Gray 1979) and 11) sea level pressure. TCG is more likely for large values of DGP, the IPV difference, 310-K IPV/IPV310-T_V, and the SGP vorticity parameter; and for small values of the 350-K IPV/IPV350-T_V, the three shear parameters, and sea level pressure.

The choice of such thermodynamic TCG metrics is informed both by concerns with GCM treatments of moist physics[2] and by GCM sensitivities to SST-related indicators of TCG (e.g., Ryan et al. 1992). The SST threshold of ~26°–27°C observed for TCG in the current climate (Evans 1993) appears to be a consequence, rather than a driver, of the present climate conditions (Dutton et al. 2000). Thus, it is important to develop thermodynamic indicators of TCG that are independent of the absolute value of the underlying SST (although they may still relate to SST spatial gradients). To minimize concerns about these SST threshold sensitivities, two parameters designed to capture the convective potential for TCG without reference to SST are examined: 12) daily averaged 500-hPa vertical velocity (W_{500}) and 13) daily averaged convective precipitation rate (PR). Consistent with the dynamical TCG metrics, to reference previous studies, we also analyze two thermodynamic parameters from the SGP: 14) the moist instability and 15) relative humidity. Two final thermodynamic parameters are considered: 16) the 500-hPa temperature at the center of the disturbance and 17) the equivalent potential temperature at 700 hPa (Table 1).

In summary, 17 metrics of TCG potential on seasonal and medium to high-frequency time scales are evaluated here (Table 1). All metrics are domain averaged over the MDR and only TCG events occurring in the MDR are used for validation of these metrics.

e. Calculation of deviation anomalies for intraseasonal metrics of TCG

To assess these TCG variables on medium to high frequencies, we develop anomalous variability metrics based on a 15-day base period. We begin by calculating daily averages of each variable over the MDR to yield 17 time series of daily and spatially averaged variables. Let **r** be a 2440 element vector of daily and spatially averaged values for an arbitrarily chosen variable from the 17-variable set. To calculate the deviation anomalies, we (i) calculate daily anomalies, r_{jt} ($j = 1, 160; t = 1, 15$) of the daily averaged values (elements of the vector **r**) compared to the 15-day mean $\bar{r}_j$, where j indexes over the set of 15-day time segments[3] and t indexes over individual days within a given time segment. (ii) Standard deviations (s_j) for each 15-day segment of these daily anomalies are calculated, $s_j = \mathrm{stdev}(r_{jt})$, and (iii) the standard deviation $\bar{s}$ for all of the 15-day periods over the 20 years is computed via

---

[2] Significant biases in the spatial distribution of precipitation in the CAM3.1 are evident, even taking into account slight overestimates of tropical Atlantic rainfall rates in the ERA-40 (Andersson et al. 2005).

[3] This analysis spans the 4-month period JJAS for each of the 20 years (1981–2000), so there are 160 × 15-day averaging time segments.

$$\bar{s} = \frac{1}{N} \sum_{j=1}^{N} s_j, \quad N = 160. \tag{3}$$

To complete the calculation of the deviation anomaly time series for the variable r, (iv) we calculate the standard deviation of the 160 15-day standard deviations $S = \mathrm{stdv}(s_j)$ and, finally, (v) subtract the 20-yr mean standard deviation $\bar{s}$ from the set of standard deviations s_j and normalize by S to recover the deviation anomalies

$$s'_j = \frac{(s_j - \bar{s})}{S}, \quad j = 1,160. \tag{4}$$

Deviation anomalies are designed to highlight anomalous variability in a single time segment ($1 \leq j \leq 160$) compared to the mean behavior for the set of all 15-day periods over the 20 years. The deviation anomaly time series form the basis for comparisons of high-frequency temporal variations between the ERA-40 and CAM3.1 datasets. They are also used as input into logistic and Poisson regression models for inference of TCG.

3. Evaluation of CAM3.1 based on existing TCG metrics

GCM skill in simulation of large-scale environmental conditions conducive for TCG on monthly and seasonal time scales is still quite variable across models (Bengtsson et al. 1995, 2007; Camargo et al. 2005). Thus, it is important to evaluate the skill of the CAM3.1 at replicating a reasonable spatial distribution of the conditions conducive to TCG before exploring the tropical high-frequency variability. To do this, we calculate spatial distributions of the monthly SGP [Eq. (1), Fig. 1] and monthly GPI [Eq. (2), Fig. 3] from the ERA-40 for September over the period 1981–2000.

a. Seasonal and monthly time scales: The SGP and GPI

In the first stage of the CAM3.1 validation analysis, the individual terms and the aggregate values for both SGP and GPI equations are calculated by month. The June–September (JJAS) means and September-only means are used for (i) validation of the diagnostics from the ERA-40 against the observed TCG record and (ii) evaluation of the four-member CAM3.1 ensemble. Diagnostics of each genesis metric includes evaluations of their spatial distributions for (i) a single month and year, (ii) the variance of the monthly means, and (iii) the 20-yr mean and variance. These calculations are performed for the entire North Atlantic basin, for the MDR alone, and for a larger tropical band: 9°–21°N, 20°–80°W

(Waters 2011). Results for the basinwide and MDR analyses are reported here.

The SGP fields for the ERA-40 and one of the CAM3.1 ensemble members[4] are comparable in magnitudes (Figs. 1a and 1b). High likelihoods (yellow and red regions) signifying multiple TCG events are identified in both the MDR and southern Gulf of Mexico, but a larger region conducive for TCG events (the north-central Atlantic and the majority of the gulf) is evident in the ERA-40 (Fig. 1a). Further, the TCG maximum off equatorial West Africa is well captured in the ERA-40 SGP (Fig. 1a), but in the CAM3.1 this maximum is shifted farther west into the central equatorial Atlantic (Fig. 1b). Comparisons of the SGP component terms (Figs. 1c–l) provide an explanation for the sources of these discrepancies between the reanalyses and the AGCM. The spatial distributions of the dynamic variables, the scaled relative vorticity term [Eq. (1); Figs. 1c,d], and the inverse shear term (Figs. 1e,f) are generally comparable. However, a small adverse vorticity region in the eastern Caribbean is noticeable in the ERA-40 that is not present in the CAM3.1. Similarly, a favorable shear environment in the north-central Atlantic evident in the ERA-40 is not replicated in the CAM3.1 simulation. Ocean thermal energy signatures are also comparable across both models. The major differences lie in the other thermodynamic variables: the instability and the $RH_{700-500}$ parameters. Although the pattern of moist instability is consistent between the two (Figs. 1i and 1j), the magnitude of the CAM3.1 field is substantially weaker. Likewise, CAM3.1 is much drier off of the West African coast, in the northern gulf, and out into the central North Atlantic. In summary, the major differences between the CAM3.1 ensemble and ERA-40 (based on the monthly averaged spatial distributions of SGP diagnostics) are derived from discrepancies in the thermodynamic parameters.

Examination of the variance of the 20-yr MDR-averaged SGP and each of the SGP component parameters reveals that the moist instability, relative humidity, and shear terms in the ERA-40 are significantly more variable than those in the CAM3.1 ensemble (Table 2). Overall, the SGP variance in the ERA-40 is triple that calculated for any of the CAM3.1 ensemble members, while the four CAM3.1 ensemble members have very

---

[4] The analyses are performed for each of the four ensemble members. Although each member yields slightly different magnitudes of the output variables, noticeable differences are minimal (Table 2). A comparison of four variables across ERA-40 and all four ensemble members (Fig. 4) demonstrates that the CAM3.1 results plotted throughout are representative of the ensemble results more generally. However, for brevity, we generally plot only one ensemble member.
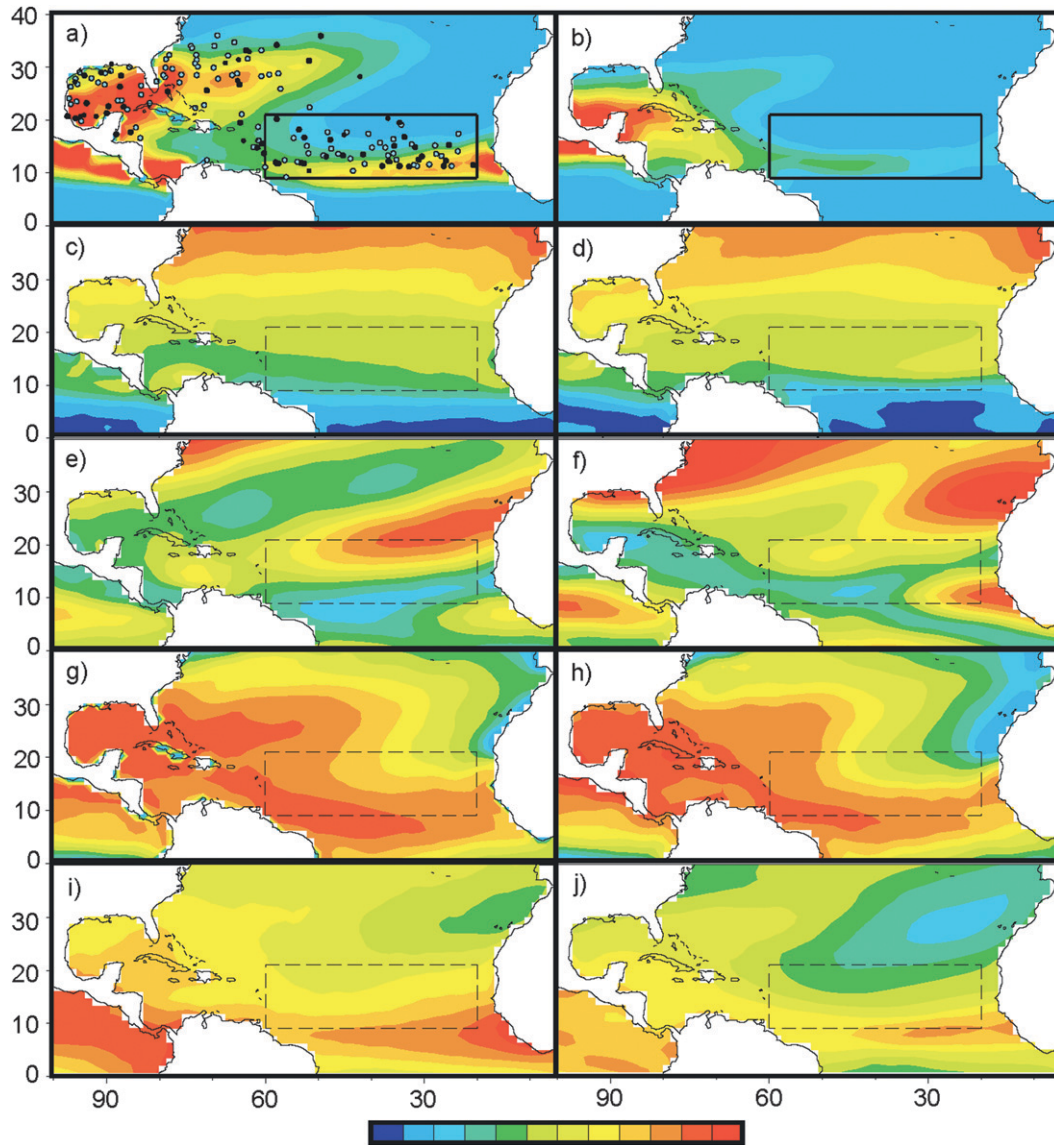
FIG. 3. GPI and component terms for the 1981–2000 mean September: (a),(b) GPI output (number of potential TCG events totaled over the 20 Septembers), (c),(d) 850-hPa absolute vorticity parameter (s^{-1}), (e),(f) 200–850-hPa shear parameter (m s^{-1}), (g),(h) potential intensity (PI) parameter (m s^{-1}), and (i),(j) 700-hPa relative humidity parameter (%). GPI values range from 0 to 10, absolute vorticity values from 0 to 10 ($\times 10^{-5}$ s^{-1}), shear magnitudes from 0 to 20 m s^{-1}, PI values up to 20 m s^{-1}, and RH values from 0% to 80%. Lower numbers (blue shading) indicate the least favorable conditions for TCG events and higher numbers (orange and red) indicate the most favorable conditions for TCG events. The MDR and TCG locations are plotted as described for Fig. 1.

similar variance ranges for each SGP component; for instance, variance of the CAM3.1 SGP is only O(0.17–0.18) compared to 0.58 for the ERA-40 (Table 2).

We also use the GPI [Eq. (2)] and its components (see ftp://texmex.mit.edu/pub/emanuel/TCMAX/pcmin_revised.f for the potential intensity routine) to repeat this comparison of the monthly averaged conditions conducive to TCG (Fig. 3). As with the SGP, the spatial distributions of the dynamical variables, absolute vorticity (Figs. 3c,d),

and shear (Figs. 3e,f) are comparable, although the CAM3.1 now has slightly stronger shear off West Africa in addition to the north-central Atlantic (Fig. 3f). Also consistent with the SGP, the magnitude of the thermodynamic relative humidity parameter is weaker for the CAM3.1 with drier RH (Fig. 3j) compared to the ERA-40 (Fig. 3i). Potential intensity (PI) output from both ERA-40 (Fig. 3g) and CAM3.1 (Fig. 3h) simulations are comparable. A tropical precipitation bias that has been identified in

TABLE 2. Main development region variance in the months June–September of the 20 years (1981–2000) for the ERA-40 reanalyses and CAM3.1 AGCM ensemble members expressed in terms of (top) the SGP and its component terms and (bottom) the GPI and the physical variables making up its component terms. PI calculations are based on Emanuel (1995). MDR ocean thermal energy is the same for all of the CAM3.1 ensemble members, since SSTs were prescribed in this AGCM.

| | ERA-40 | CAM3.1 ensemble members | | | |
		IC1	IC2	IC3	IC4
		SGP and component terms			
Relative vorticity at 850-hPa	7.3×10^{-13}	1.6×10^{-12}	1.8×10^{-12}	1.6×10^{-12}	1.7×10^{-12}
Moist instability: surface to 500 hPa	1.8	1.0	1.0	1.1	1.2
Ocean thermal energy	8.9×10^{6}	9.6×10^{6}	9.6×10^{6}	9.6×10^{6}	9.6×10^{6}
Relative humidity from 700 to 500 hPa	16.8×10^{-3}	7.8×10^{-3}	8.0×10^{-3}	8.4×10^{-3}	9.0×10^{-3}
Inverse shear: 200 to 925-hPa	7.5×10^{-4}	2.0×10^{-4}	2.5×10^{-4}	2.1×10^{-4}	2.7×10^{-4}
SGP	**0.58**	**0.18**	**0.17**	**0.17**	**0.17**
		GPI and component terms			
Absolute vorticity at 850 hPa	6.1×10^{-12}	1.7×10^{-12}	1.3×10^{-12}	1.4×10^{-12}	1.4×10^{-12}
Potential intensity	53.5	84.1	77.7	80.1	82.8
Relative humidity at 700 hPa	29.0	41.9	43.4	44.6	45.1
Shear: 200 to 850 hPa	18.3	1.8	3.3	2.1	2.7
GPI	**1.75**	**0.19**	**0.21**	**0.18**	**0.23**

the ERA-40 (Andersson et al. 2005) could also provide a partial explanation for these discrepancies.

As with the SGP, the ERA-40 GPI and its components are much more variable than any of the CAM3.1 ensembles (Table 2): three of the four ERA-40 GPI components are over twice as variable and the ERA-40 GPI is almost an order of magnitude larger than the CAM3.1 GPI. Again, the range of variance for all GPI terms is small for all CAM3.1 ensemble members.

The capabilities and limitations of the CAM3.1 ensemble runs to simulate the monthly and seasonal variations in large-scale environmental indicators of TCG potential (Figs. 1 and 3), and the lower variability of the CAM3.1 compared to the ERA-40 reanalysis (Table 2), are identified in the analyses presented here. Taking all of these factors into consideration, we conclude that CAM3.1 is capable of reasonably simulating conditions conducive for TCG on seasonal time scales.

b. CAM3.1 representation of additional metrics of daily and monthly TCG potential

Having evaluated the CAM3.1 tropical atmosphere using monthly means and variances of the SGP and GPI diagnostics, we now employ additional metrics to explore the skill of the CAM3.1 at capturing the daily and monthly variability of TCG potential (Table 1).

Thermodynamic parameters in the SGP and the GPI combine to identify regions that could support active deep convection (Evans 2011). Our choice of additional thermodynamic TCG predictors focuses on identifying modulation of active deep convection on monthly time scales via monthly averaged convective precipitation rate (PR), pressure vertical velocity (W_{500}), 500-hPa

temperature (T_{500}), and moisture availability ($RH_{700-500}$) (Table 1); the September mean ERA-40 and CAM3.1 spatial distributions of these variables are illustrated from 1981 to 2000 (Fig. 4). Regions of deep convective activity (PR > 8 mm day^{-1}; Figs. 4a,e,i,m,q) and strong vertical ascent (Figs. 4b,f,j,n,r) are evident in the MDR, gulf, and north-central Atlantic; however, compared to ERA-40 (Figs. 4a–d), the CAM3.1 ensemble members depict a more "ITCZ-like" structure of deep convection (especially in the MDR; Figs. 4e,i,m,q), yields comparable W_{500} throughout the tropical Atlantic (Figs. 4f,j,n,r), overestimates T_{500} throughout the tropical Atlantic and Gulf (Figs. 4g,k,o,s), and underestimate the $RH_{700-500}$ magnitudes in the Gulf (Figs. 4h,l,p,t). Notably, while there is clearly variability among the CAM3.1 ensemble members, the spatial structures and magnitudes are relatively similar. Overall, comparison of these indicators of moist convective activity in CAM3.1 with ERA-40 demonstrates that the CAM3.1 has skill in discriminating regions of enhanced convective potential.

Dynamic TCG potential on daily time scales is diagnosed in terms of low-level cyclonic vorticity and convergence, upper-level anticyclonic vorticity and divergence, and weak shear profiles (McBride and Zehr 1981). Since the convergence–divergence dipole between the lower and upper troposphere signifies convection in the core of the TC (e.g., Evans 2011), we summarize these dynamical TCG indicators as daily values of low-level IPV310, upper-level IPV350, and three shear metrics (Table 1). Comparisons of these fields diagnosed from the ERA-40 for days when an Atlantic TC was present with the National Hurricane Center (http://www.nhc.noaa.gov/pastall.shtml)-observed best tracks [the North Atlantic
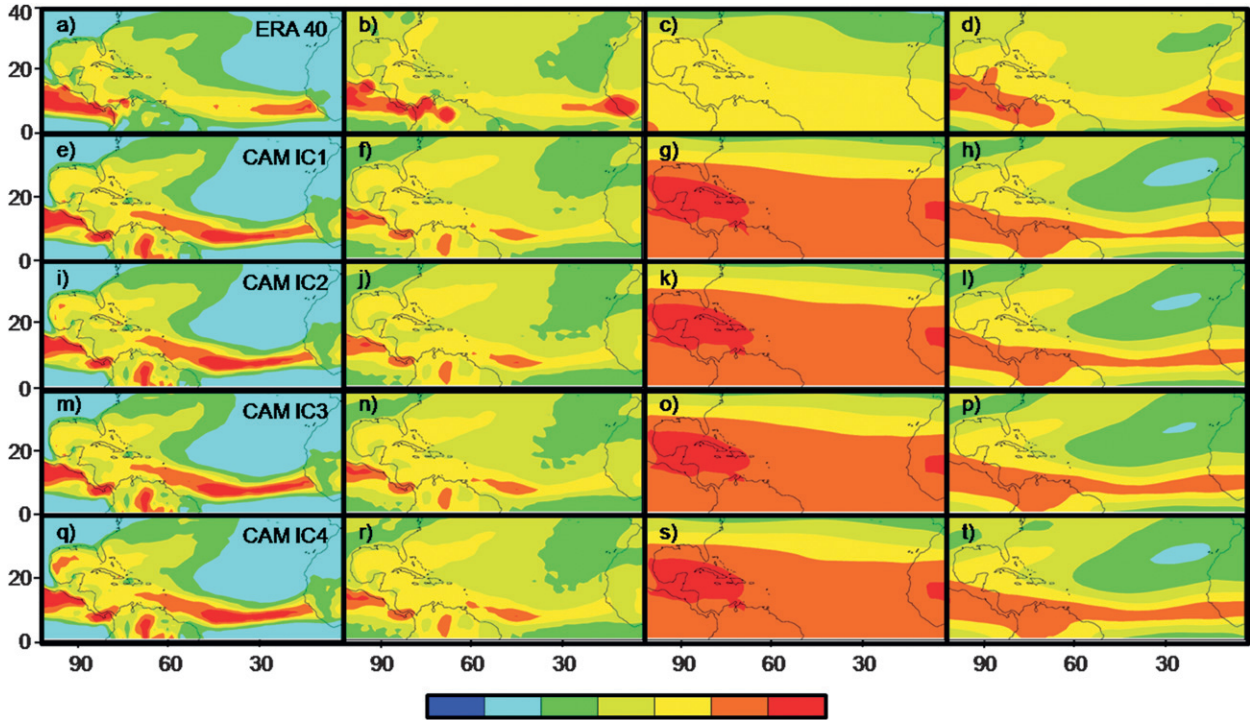
FIG. 4. Comparison of 1981–2000 monthly averaged September thermodynamic metrics (Table 1) for (top row) ERA-40 and (lower rows) each of the CAM3.1 ensemble members: (from left to right) convective precipitation rate (PR, mm day^{-1}), 500-hPa vertical velocity W_{500} (hPa day^{-1}), 500-hPa temperature T_{500} (K), and midtropospheric relative humidity RH$_{700-500}$ (%).

hurricane database (HURDAT)] confirms that the ERA-40 diagnostics are reasonable metrics for daily TCG potential.

The 20-yr simulation of the CAM3.1 cannot be expected to validate in day-by-day comparisons but should produce spatial patterns and modes of variability consistent with the observed local weather and climate. Comparisons of these daily dynamical metrics from CAM3.1 with ERA-40 (not shown) reveal that the magnitudes of the shear terms and IPV350 are similar between the two. CAM3.1 develops low-level vortices of similar spatial scales to those analyzed in ERA-40, but the magnitudes of these IPV310 signatures are smaller.

4. Principal component analysis on subseasonal TCG data

To focus on the variability of the large-scale environment as the signature of TCG, we calculate deviation anomalies averaged over the entire MDR (section 2e) for each baseline 15-day period. These deviation anomalies are calculated for the ERA-40 and each of the CAM3.1 ensemble members for all 17 candidate variables (Table 1). We perform principal component analysis (e.g., Von Storch and Zwiers 1999) on a correlation

matrix created from the vector $\mathbf{x}$ of deviation anomalies calculated for all input variables. This approach is designed to remove redundancies among the input variable set and to develop a reduced set of orthogonal composite principal component (PC) vectors to use as inputs to the new TCG summary metrics described in section 5. Each PC is defined by an eigenvector comprising elements (loading values) that are linear combinations of $\mathbf{x}$ (Wilks 2006, 463–466). Thus, the mth PC u_m is the projection of $\mathbf{x}$ onto the mth eigenvector $\mathbf{e}_m$:

$$u_m = \mathbf{e}_m^{\mathrm{T}}\mathbf{x} = \sum_{k=1}^{K} e_{km}x_k, \quad m = 1, \ldots, M. \quad (5)$$

Here, each of the M eigenvectors contains one loading value pertaining to each of the K variables, x_k. The first eigenvector points in the direction in which $\mathbf{x}$ exhibits the most joint temporal variability. Subsequent eigenvectors are perpendicular to all previous eigenvectors and locate directions in which the original data displays maximum remaining joint temporal variability. Thus, all PCs are mutually uncorrelated and account successively for the maximum joint variability of $\mathbf{x}$. We retain the subset of PCs for the ERA-40 and additional PC subsets for each CAM3.1 ensemble member that explain at least 70% of the combined variance.
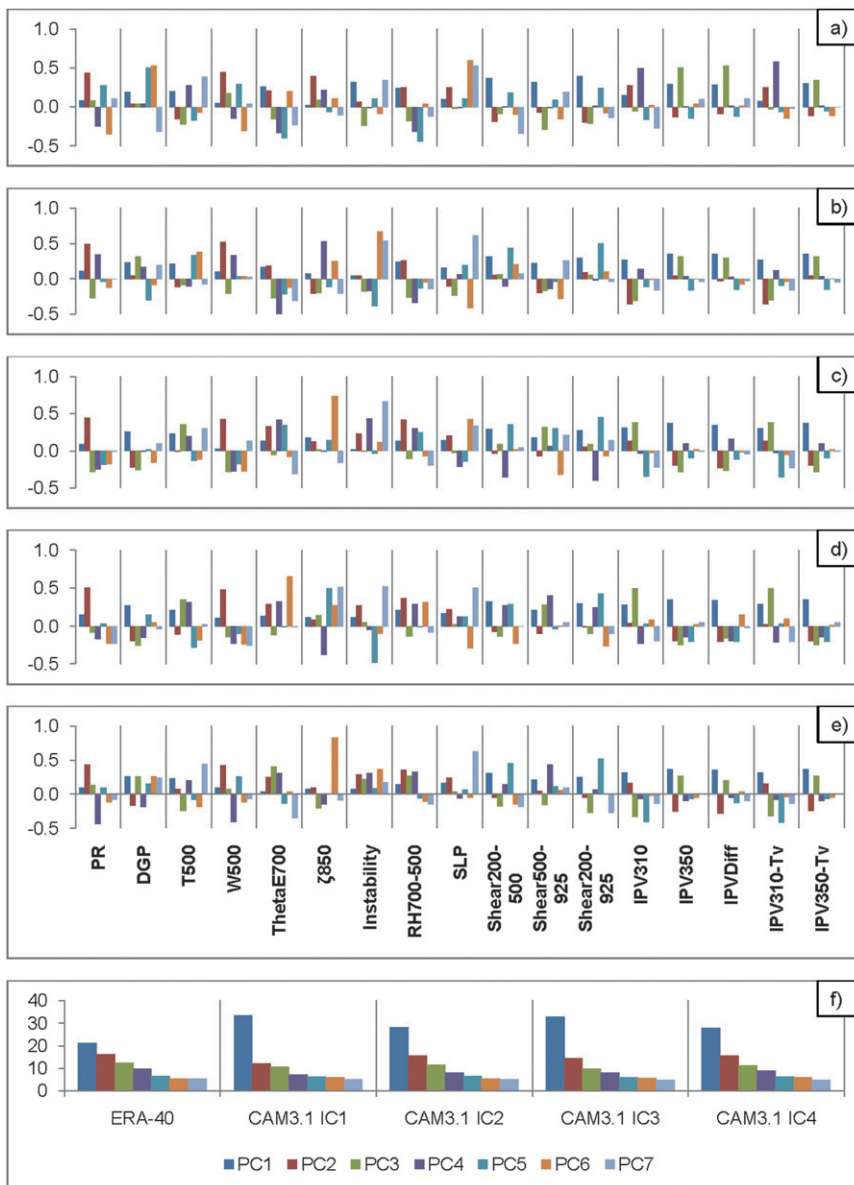
FIG. 5. Variable loadings for each of the first seven principal components (color coded) diagnosed in (a) the ERA-40 and (b)–(e) the four CAM3.1 ensemble members. An individual PC is constructed by multiplying the value indicated by the corresponding bar with the variable and summing across all variables to recover the linear combination as given in Eq. (5); (f) percent variance explained for each PC for (from left to right) the ERA-40 and each CAM3.1 ensemble members are plotted.

The loading values in each PC (plotted by variable for the ERA-40 and each of the four CAM3.1 ensemble members in Fig. 5) are examined to determine the dominant dynamic and/or thermodynamic contributors to each PC. Having established the dominant contributors to each PC, we examine the dominant contributors to each PC for the ERA-40 and the CAM3.1 ensemble members to compare their dominant sources of variability in the MDR.

Intercomparison of the variables in ERA-40 and CAM3.1 dominating the variance explained by the individual PCs provides insights into the sources for the discrepancies highlighted by the SGP (Fig. 1) and GPI (Fig. 3) diagnostics. PC1 and PC2 show similar dependencies across all ERA-40 and CAM3.1 analyses, but there is less consistency of variable contributions to PC3 through PC7 (Fig. 5). The first PC of the ERA-40

captures variability in the upper-level IPV (IPV350, IPV350-Tv, and IPVDiff) and shear (Shear200–500, Shear500–925, and Shear200–925) terms. The effects of convection are evident in PC2 via PR and W_{500} and indirectly through ζ_{850}, which will act to reduce the Rossby radius and, thus, enhance the effects of the convection locally. Although these ERA-40 dependencies for PC1 and PC2 are generally repeated in each of the CAM3.1 ensemble members, some differences are evident. For example, all CAM3.1 members have similar loading values for the DGP and all five IPV terms in PC1, indicating a notable inability of the CAM3.1 to differentiate between upper-level and lower-level dynamic rotational variability. Similarly, in PC2 all CAM3.1 members identify the dominant covariance between PR and W_{500} but do not capture a link to ζ_{850}.

Dynamic terms dominate the weaker PCs retained (PC3–PC7) for the ERA-40, with the thermodynamic terms playing a supporting role at best. PC3 is most influenced by IPV in the upper troposphere, while PC4 captures lower-tropospheric IPV variability, with a weaker (negative) dependence on the moisture variables $RH_{700–500}$ and ThetaE700. PC5 has the strongest contribution from the DGP, but once again $RH_{700–500}$ and ThetaE700 play a supporting role. SLP provides a major influence on PC6, but the DGP is also a strong contributor, with the convective terms PR and W_{500} also contributing to the variance explained by this PC. The variability in PC7 is dominated by SLP.

The CAM3.1 PC3–PC7 yield a more uniform distribution of similar dynamic and thermodynamic terms. Three of the four members capture the dominant variability and covariability of the dynamic terms (i.e., IPV terms, SLP) evident in the ERA-40, but the thermodynamic variables—ThetaE700, instability, and $RH_{700–500}$—that contributed weakly to the ERA-40 PC play a much stronger role here. These results suggest that the thermodynamic terms vary more on the 15-day time scale in CAM3.1 than in ERA-40.

Results from this analysis indicate several important capabilities and limitations of the CAM3.1 for capturing subseasonal MDR variability. All CAM3.1 members exhibit similar dependencies (variable loadings) to the ERA-40 for PC1 and PC2. However, the CAM3.1 ensemble members uniformly capture a stronger contribution of the thermodynamic terms in PC3–PC7 and downplay the influence of other dynamic variables, such as DGP and SLP, in explaining temporal variability on the 15-day time scale within the MDR. The variance explained by PC1 in all CAM3.1 members is much higher than that for the ERA-40, consistent with the reduced variability in this AGCM (Table 2).

5. Development of regression models for TCG in the MDR

The resolution of the CAM3.1 simulations analyzed here ($1.4° \times 1.4°$) is too coarse to capture the details of genesis, so we need to infer TC activity from the GCM fields. The distinction between this study and earlier works of this kind is that the composite metrics developed here directly incorporate measures of daily anomalous variability within 15-day periods (section 2e) of each variable of interest. Using the first seven PCs calculated from the PCA applied to the ERA-40 large-scale fields (section 4), we develop two regression models to assess how well the high-frequency variability is associated with (i) observed TCG events (≥ 1; logistic regression model) and (ii) multiple observed TCG events (≥ 1, Poisson regression model) within the MDR domain in a given 15-day time period. The seven PCs are chosen because they explain a sufficient amount of temporal variance of the original deviation anomalies that we deemed appropriate. Furthermore, this choice of employing the PCs as the predictor set reflects our initial hypothesis that information on short-time-scale variability is necessary for skillful TCG detection. Thus, the skill of these regression models provides information on the relative importance of measures of high-frequency variability in detecting TCG within the MDR. This regression method is not a predictive tool, but a step toward developing a diagnostic for inferring TCG likelihood in GCMs that utilizes variability metrics of the genesis environment. We do not create regression models based on the CAM3.1 because to do so we would have needed to simulate TCG and TC events within the AGCM, which strays from the goals of this paper. However, given the CAM3.1 skill in simulating seasonality and medium- to high-frequency variability signatures (sections 3 and 4), we hypothesize that a regression model determined from the ERA-40 could be applied to the CAM3.1 to infer TCG likelihoods. We report on the results from both regression models here.

a. Logistic regression using reanalysis data

We first develop a logistic regression model to assess the diagnostic capabilities of the ERA-40-based PCs (predictors) to detect observed TCG occurrences (predictand, Fig. 2) on the 15-day time scales. In the process of logistic regression, we fit a logit probability function, $p_i = (1 + e^{-z_i})^{-1}$, $i = 1, N$, where N is the number of 15-day time periods, using logistic regression to the predictors x_k (the seven leading PCs) for a known set of outcomes Z_i [the binary predictand: TCG yes (Y) or no (N; see Fig. 2] by maximizing the log-likelihood
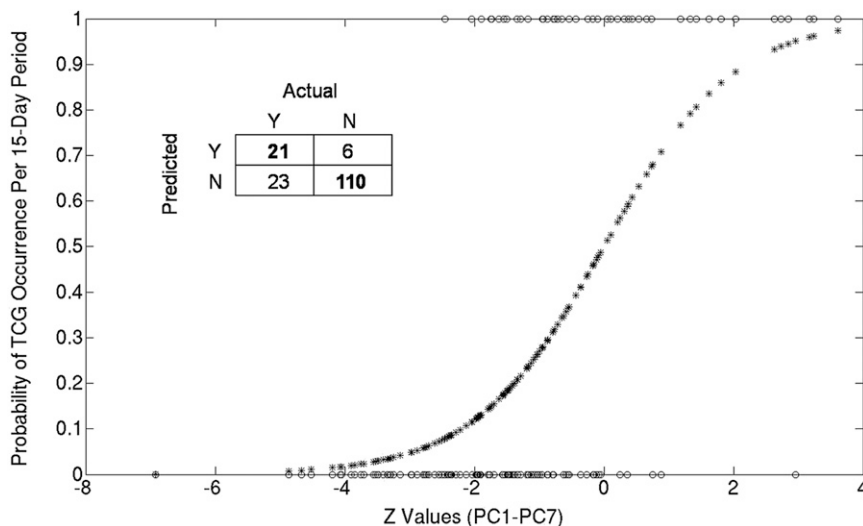
FIG. 6. Performance of the TCG logistic regression model based on 15-day deviation anomalies from the ERA-40. Observed genesis (or nongenesis) events (open circles); the resulting logistic regression model indicating the likelihood of a TCG occurrence for a given value of Z (derived from the large-scale deviation anomalies) is plotted (asterisk line). The inset is the confusion matrix summary of these results. The confusion matrix statistics are compiled using a threshold probability of 0.5 to designate a TCG event forecast by the regression model.

$$\ln\left(\frac{p_i}{1-p_i}\right) = b_0 + b_1 x_{1i} + \cdots + b_k x_{ki} = Z_i, \qquad (6)$$

where $(b_0, b_1, b_2, \ldots, b_k)$ are the regression parameters. Using this technique, the regression estimates become bounded on the interval [0, 1] in the form of an S-shaped curve (Fig. 6).

To evaluate our logistic regression model, we determine that genesis will be detected for $p \geq 0.5$ and will not be detected for $p < 0.5$. We summarize these results in a 2×2 confusion matrix (inset in Fig. 6). A variety of skill metrics can be evaluated (Wilks 2006) from the information summarized in the confusion matrix: we employ accuracy, precision, threat score, and hit rate to evaluate this model (Table 3).

The logistic regression model (Fig. 6) correctly detects (YY or NN in the confusion matrix) 131 of the 160 events, yielding an accuracy of 82%. Similarly, 21 of the 27 TCG predictions are verified, corresponding to a model precision of 78%. Based on these statistics, the model appears to be performing at an exemplary level. However, threat score and hit rate also take into account false alarms (Table 3) and thus provide a more rigorous test of model skill. This model achieves a threat score of 42% and hit rate of 48%. So, even by the most stringent skill metrics commonly used, this large-scale variability-based model correctly identifies TCG occurrences in the period almost 50% of the time.

b. Poisson regression

A Poisson regression model was developed to determine the diagnostic capabilities of high-frequency variability at detecting multiple TCG events in a 15-day window (Fig. 7). Using the same seven ERA-40 PCs as predictors, we calculate the conditional mean μ_i of the predictand (number of events); μ_i, modeled as a Poisson random variate dependent on the seven PC predictors fit to the predictand of genesis, counts using the same log-likelihood method for estimation of the fitting parameters as employed for the logistic regression [Eq. (6)]. To

TABLE 3. Skill metrics used in the evaluation of the logistic and Poisson regression models. Statistics for the outcomes are provided in the confusion matrix inset in Figs. 6 and 7. Outcomes are interpreted as YY: TCG is forecast and observed, YN: TCG is forecast but does not occur (false alarm), NY: TCG is observed but is not forecast (miss), and NN: TCG is not forecast and does not occur.

Skill metric	Definition
Accuracy	Proportion of correct predictions from all predictions
Precision	Proportion of correct positives from all positive predictions
Skill score	Proportion of correct true forecasts from all occasions that event was either forecasted or observed
Threat rate	Proportion of correct true forecasts to the number of events observed
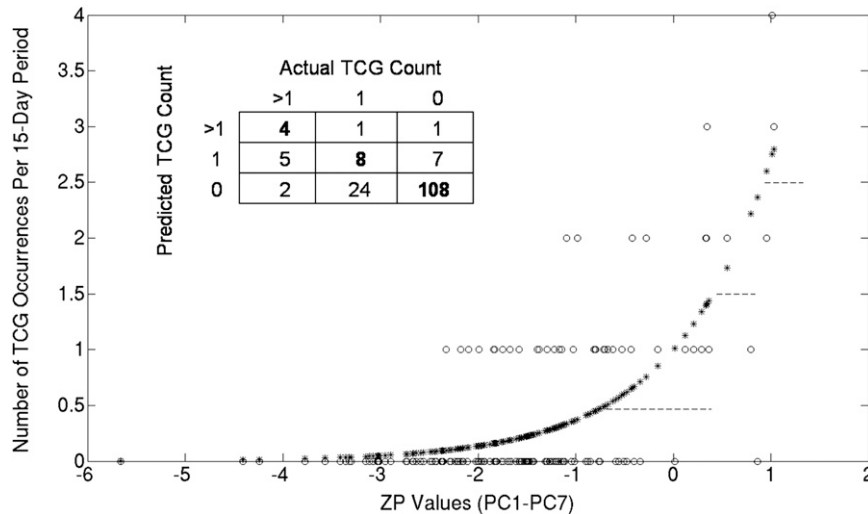
FIG. 7. Performance of the TCG Poisson regression model based on 15-day deviation anomalies from the ERA-40. Observed genesis (or nongenesis) events (open circles), and the Poisson regression model indicating the number of TCG events likely to occur for a given value of Z (derived from the large-scale deviation anomalies) is plotted as asterisks. The inset is the confusion matrix summary of these results. The confusion matrix statistics are compiled using a threshold probability of 0.5 to designate a TCG event forecast by the regression model.

evaluate the Poisson model skill at identifying a plurality of TCG events, we construct a 3×3 confusion matrix for TCG count ranges 0, 1, >1. As with the logistic regression model, TCG was determined to be detected if the number of projected occurrences exceeded 0.5 and the forecast TCG count was incremented at 1.5 (two events), 2.5 (three events), and 3.5 (four events); no 15-day period had more than four events.

Threat score and hit rate data indicate a weak predictive skill of the PC combinations to detect observed TCG counts in a given 15-day period: threat scores and hit rates are comparable for the non TCG (67% and 96%) and single TCG occurrences (16% and 24%), but improved for TCG counts greater than one (28% and 29%). Although the computed threat scores are not robust, actual TCG counts were within one of the projected TCG counts (96%). These findings suggest that the Poisson approach has the potential for increased skill if a larger TCG count database is employed, but overall weaker skill than the logistic regression (Figs. 6 and 7).

6. Summary and conclusions

In this study, we assess the capabilities of an atmospheric GCM for detecting both large-scale and localized conditions for genesis in the tropical North Atlantic. We develop metrics of medium- to high-frequency (15-day base period) variability of environmental conditions and assess their utility as diagnostics of TCG in the North Atlantic MDR. We explore the hypothesis that inclusion

of information on variability, especially of the dynamic fields, will provide improved diagnostics of TCG. Diagnostics of high-frequency variability in the dynamical fields provide information on the development of potential incipient vortices as centers for TCG development.

Seventeen candidate thermodynamic and dynamic variables are identified as potential indicators of TCG activity. A four-member ensemble of the CAM3.1 atmospheric GCM is compared with observed TCG activity from 1981 to 2000 and with TCG variability metrics diagnosed from the ERA-40 dataset. The CAM3.1 is forced with observed monthly sea surface temperatures for the 20-yr period. Overall, CAM3.1 exhibits skill at simulating large-scale and localized TCG environments. Based on principal component analysis applied to CAM3.1 and ERA-40 data, CAM3.1 data exhibit distinct differences from ERA-40 data. Most of the temporal variability in the ERA-40 is explained by dynamic variability. This dominance of high-frequency variability in the dynamic fields is consistent with our hypothesis that metrics of TCG must capture information on the development of potential incipient vortices for TCG development. Although all CAM3.1 members exhibit similar primary dependencies on dynamic variability, they uniformly capture a stronger subsequent contribution of the thermodynamic terms and downplay the influence of other dynamic variables in explaining temporal variability on the 15-day time scale within the MDR.

We calculate the normalized standard deviation of daily anomalous variability from a 15-day base period for each of the 17 TCG predictors; application of PCA on the results in a set of 17 deviation anomaly time series reduces the potential indicators to a set of seven uncorrelated principal components (PCs) for TCG likelihood in the 15-day period. These seven ERA-40-based PCs are used as predictors in a logistic regression model for detection of TCG activity in the MDR. The logistic regression model yields promising accuracy (82%) and precision (78%) measures, achieving a threat score of 42% and a hit rate of 48%.

Because multiple TCG events in a given base period result in higher magnitudes of variability for that period, we develop a Poisson regression model for TCG counts based on the same seven predictors. Threat scores and hit rates for TCG counts of at least one TCG event are lower (31% and 27%, respectively) than the logistic regression model, demonstrating that weighting by TCG counts does not improve the regression model skill.

Based on these findings, there is merit in incorporating a measure of medium- to high-frequency variability (daily deviations from a 15-day base period) in metrics of TCG. The logistic regression model developed here may provide a useful tool in seasonal forecasting of TCG activity given a seasonal forecast (or ensemble of forecasts) from a dynamical numerical model. Further, given a climate model with skillful representation of seasonal and monthly large-scale environmental metrics of TCG, the logistic regression model could provide a useful diagnostic of TCG likelihood.

REFERENCES

Aiyyer, A., and J. Molinari, 2008: MJO and tropical cyclogenesis in the Gulf of Mexico and Eastern Pacific: Case study and idealized numerical modeling. *J. Atmos. Sci.,* **65,** 2691–2704.

Andersson, E., and Coauthors, 2005: Assimilation and modeling of the atmospheric hydrological cycle in the ECMWF forecasting system. *Bull. Amer. Meteor. Soc.,* **86,** 387–402.

Bengtsson, L., H. Böttger, and M. Kanamitsu, 1982: Simulation of hurricane-type vortices in a general circulation model. *Tellus,* **34,** 440–457.

——, M. Botzet, and M. Esch, 1995: Hurricane-type vortices in a general circulation model. *Tellus,* **47A,** 175–196.

——, K. I. Hodges, M. Esch, N. Keenlyside, L. Kornblueh, J.-J. Luo, and T. Yamagata, 2007: How may tropical cyclones change in a warmer climate? *Tellus,* **59A,** 539–561.

Camargo, S. J., and A. H. Sobel, 2004: Formation of tropical storms in an atmospheric general circulation model. *Tellus,* **56A,** 56–67.

——, A. G. Barnston, and S. E. Zebiak, 2005: A statistical assessment of tropical cyclone activity in atmospheric general circulation models. *Tellus,* **57A,** 589–604.

——, A. H. Sobel, A. G. Barnston, and K. A. Emanuel, 2007: Tropical cyclone genesis potential index in climate models. *Tellus,* **59A,** 428–443.

Challa, M., and R. L. Pfeffer, 1990: Formation of Atlantic hurricanes from cloud clusters and depressions. *J. Atmos. Sci.,* **47,** 909–927.

Charney, J. G., and A. Eliassen, 1964: On the growth of the hurricane depression. *J. Atmos. Sci.,* **21,** 68–75.

CISL, cited 2011: Computational and Information Systems Laboratory (CISL) Research Data Archive. [Available online at http://dss.ucar.edu/.]

Clark, J. D., and P. S. Chu, 2002: Interannual variation of tropical cyclone activity over the central North Pacific. *J. Meteor. Soc. Japan,* **80,** 403–418.

Collins, W. D., G. B. Bonan, T. B. Henderson, and D. S. McKenna, 2004: The Community Climate System Model: CCSM3. *J. Climate,* **17,** 1–30.

Dutton, J. F., C. J. Poulsen, and J. L. Evans, 2000: The effect of global climate change on the regions of tropical convection in CSM1. *Geophys. Res. Lett.,* **27,** 3049–3052.

ECMWF, cited 2011: ERA-40 background. [Available at http://www.ecmwf.int/research/era/do/get/era-40.]

Emanuel, K. A., 1986: An air–sea interaction theory for tropical cyclones. Part I: Steady-state maintenance. *J. Atmos. Sci.,* **43,** 585–605.

——, 1995: Sensitivity of tropical cyclones to surface exchange coefficients and a revised steady-state model incorporating eye dynamics. *J. Atmos. Sci.,* **52,** 3969–3976.

——, and D. Nolan, 2004: Tropical cyclone activity and global climate. Preprints, *26th Conf. on Hurricanes and Tropical Meteorology,* Miami, FL, Amer. Meteor. Soc., 10A.2. [Available online at https://ams.confex.com/ams/pdfpapers/75463.pdf.]

——, R. Sundararajan, and J. Williams, 2008: Hurricanes and global warming: Results from downscaling IPCC AR4 simulations. *Bull. Amer. Meteor. Soc.,* **89,** 347–367.

Evans, J. L., 1993: Sensitivity of tropical cyclone intensity to sea surface temperature. *J. Climate,* **6,** 1133–1140.

——, 2011: Chapter 8: Tropical cyclones. *Introduction to Tropical Meteorology,* version 2.0, A. Laing and J. L. Evans, Eds., COMET. [Available online at http://www.meted.ucar.edu/tropical/textbook_2nd_edition/index.htm.]

Frank, W. M., and P. E. Roundy, 2006: The role of tropical waves in tropical cyclogenesis. *Mon. Wea. Rev.,* **134,** 2397–2417.

Gall, J. S., I. Ginis, S.-J. Lin, T. P. Marchok, and J.-H. Chen, 2011: Experimental tropical cyclone prediction using the GFDL 25-km-resolution global atmospheric model. *Wea. Forecasting,* **26,** 1008–1019.

Goldenberg, S. B., and L. J. Shapiro, 1996: Physical mechanisms for the association of El Niño and West African rainfall with Atlantic major hurricane activity. *J. Climate,* **9,** 1169–1187.

Gray, W. M., 1968: Global view of the origin of tropical disturbances and storms. *Mon. Wea. Rev.,* **96,** 669–700.

——, 1979: Hurricanes: Their formation, structure and likely role in the tropical circulation. *Meteorology over the Tropical Oceans,* D. B. Shaw, Ed., Royal Meteorological Society, 155–218.

——, 1988: Environmental influences on tropical cyclones. *Aust. Meteor. Mag.,* **36,** 127–138.

Knutson, T. R., J. J. Sirutis, S. T. Garner, I. M. Held, and R. E. Tuleya, 2007: Simulation of the recent multidecadal increase of Atlantic hurricane activity using an 18-km-grid regional model. *Bull. Amer. Meteor. Soc.,* **88,** 1549–1565.

LaRow, T. E., Y.-K. Lim, D. W. Shin, E. P. Chassignet, and S. Cocke, 2008: Atlantic basin seasonal hurricane simulations. *J. Climate,* **21,** 3191–3206.

McBride, J. L., and R. Zehr, 1981: Observational analysis of tropical cyclone formation. Part II: Comparison of nondeveloping versus developing systems. *J. Atmos. Sci.,* **38,** 1132–1151.

McDonnell, K. A., and N. J. Holbrook, 2004: A Poisson regression model of tropical cyclogenesis for the Australian–southwest Pacific Ocean region. *Wea. Forecasting,* **19,** 440–455.

Montgomery, M. T., and B. F. Farrell, 1993: Tropical cyclone formation. *J. Atmos. Sci.,* **50,** 285–310.

Oouchi, K., J. Yoshimura, H. Yoshimura, R. Mizuta, S. Kusunoki, and A. Noda, 2006: Tropical cyclone climatology in a global-warming climate as simulated in a 20km-mesh global atmospheric model: Frequency and wind intensity analyses. *J. Meteor. Soc. Japan,* **84,** 259–276.

Ooyama, K., 1964: A dynamical model for the study of tropical cyclone development. *Geofis. Int.,* **4,** 187–198.

Randall, D. A., and Coauthors, 2007: Climate models and their evaluation. *Climate Change 2007: The Physical Science Basis,* S. Solomon et al., Eds., Cambridge University Press, 589–662.

Royer, J.-F., F. Chauvin, B. Timbal, P. Araspin, and D. Grimal, 1998: A GCM study of the impact of greenhouse gas increase on the frequency of occurrence of tropical cyclones. *Climatic Change,* **38,** 301–343.

Ryan, B. F., I. G. Watterson, and J. L. Evans, 1992: Tropical cyclone frequencies inferred from Gray's yearly genesis parameter: Validation of GCM tropical climates. *Geophys. Res. Lett.,* **19,** 1831–1834.

Schubert, W. H., S. A. Hausman, M. Garcia, K. V. Ooyama, and H.-C. Kuo, 2001: Potential vorticity in a moist atmosphere. *J. Atmos. Sci.,* **58,** 3148–3157.

Smirnov, D., and D. J. Vimont, 2011: Variability of the Atlantic Meridional Mode during the Atlantic hurricane season. *J. Climate,* **24,** 1409–1424.

Sobel, A. H., E. D. Maloney, G. Bellon, and D. M. Frierson, 2009: Surface fluxes and tropical intraseasonal variability: A reassessment. *J. Adv. Model. Earth Syst.,* **2,** 1–27.

Straub, K. H., P. T. Haertel, and G. N. Kiladis, 2010: An analysis of convectively coupled Kelvin waves in 20 WCRP CMIP3 global coupled climate models. *J. Climate,* **23,** 3031–3056.

Thorncroft, C., and I. Pytharoulis, 2001: A dynamical approach to seasonal prediction of Atlantic tropical cyclone activity. *Wea. Forecasting,* **16,** 725–734.

Vecchi, G. A., and B. J. Soden, 2007: Increased tropical Atlantic wind shear in model projections of global warming. *Geophys. Res. Lett.,* **34,** L08702, doi:10.1029/2006GL028905.

——, M. Zhao, H. Wang, G. Villarini, A. Rosati, A. Kumar, I. M. Held, and R. Gudgel, 2011: Statistical–dynamical predictions of seasonal North Atlantic hurricane activity. *Mon. Wea. Rev.,* **139,** 1070–1082.

Vitart, F., 2006: Seasonal forecasting of tropical storm frequency using a multi-model ensemble. *Quart. J. Roy. Meteor. Soc.,* **132,** 647–666.

——, J. L. Anderson, and W. F. Stern, 1997: Simulation of interannual variability of tropical storm frequency in an ensemble of GCM integrations. *J. Climate,* **10,** 745–760.

——, and Coauthors, 2007: Dynamically-based seasonal forecasts of Atlantic tropical storm activity issued in June by EUROSIP. *Geophys. Res. Lett.,* **34,** L16815, doi:10.1029/2007GL030740.

Von Storch, H., and F. W. Zwiers, 1999: *Statistical Analysis in Climate Research.* Cambridge University Press, 495 pp.

Walsh, K., and I. G. Watterson, 1997: Tropical cyclone-like vortices in a limited area model: Comparison with observed climatology. *J. Climate,* **10,** 2240–2259.

Waters, J., 2011: Towards improving the detection of North Atlantic tropical cyclogenesis (TCG). M.S. thesis, Department of Meteorology, The Pennsylvania State University, 112 pp.

Watterson, I. G., J. L. Evans, and B. F. Ryan, 1995: Seasonal and interannual variability of tropical cyclogenesis: Diagnostics from large scale fields. *J. Climate,* **8,** 3052–3065.

Wehner, M. F., G. Bala, P. Duffy, A. A. Mirin, and R. Romano, 2010: Towards direct simulation of future tropical cyclone statistics in a high resolution global atmospheric model. *Adv. Meteor.,* **2010,** 915303, doi:10.1155/2010/915303.

Wilks, D. S., 2006: *Statistical Methods in the Atmospheric Sciences.* 2nd ed. Elsevier, 627 pp.

Yokoi, S., Y. N. Takayabu, and J. C.-L. Chan, 2009: Tropical cyclone genesis frequency over the western North Pacific simulated in medium-resolution coupled general circulation models. *Climate Dyn.,* **33,** 665–683.

Zhang, Y., S. Klein, J. Boyle, and G. G. Mace, 2010: Evaluation of tropical cloud and precipitation statistics of Community Atmosphere Model version 3 using CloudSat and CALIPSO data. *J. Geophys. Res.,* **115,** D12205, doi:10.1029/2009JD012006.

Zhao, M., and I. M. Held, 2010: An analysis of the effect of global warming on the intensity of Atlantic hurricanes using a GCM with statistical refinement. *J. Climate,* **23,** 6382–6393.

——, ——, S.-J. Lin, and G. A. Vecchi, 2009: Simulations of global hurricane climatology, interannual variability, and response to global warming using a 50-km resolution GCM. *J. Climate,* **22,** 6653–6678.